Nanoparticle Size Effects for Computed Phase Equilibria in Molybdenum and Tungsten Carbides

---

A Thesis

Presented to

the faculty of the School of Engineering and Applied Science

University of Virginia

---

in partial fulfillment
of the requirements for the degree

Master of Science

by

Xutao Gao

May 2020

APPROVAL SHEET

This Thesis
is submitted in partial fulfillment of the requirements
for the degree of
Master of Science

Author Signature: Xutao Gao

This Thesis has been read and approved by the examining committee:

Advisor: Christopher Paolucci

Committee Member: Gaurav Giri

Committee Member: Joshua J. Choi

Committee Member: William Epling

Committee Member: Bi-Cheng Zhou

Committee Member:

Accepted for the School of Engineering and Applied Science:

Craig H. Benson, School of Engineering and Applied Science

May 2020

Abstract

Transition metal carbides (TMC) are important materials for a variety of applications and industrial processes, in part due to their variable crystal structures. However, the nucleation of TMC during synthesis often proceeds through metastable phases, the appearance of which, cannot be described by traditional density functional theory (DFT) computed phase diagrams. Knowledge of the relative thermodynamic stability of non-equilibrium phases during carbide synthesis could be used to guide rational design of synthetic strategies that target specific phases for individual applications. In this thesis, by combining classical nucleation theory and DFT-computed phase diagrams, we construct particle size-dependent phase diagrams for TMCs to reveal the relationships between phase stability and TMC nanoparticle size. We compute size-dependent phase diagrams for a range of molybdenum carbide and tungsten carbide stoichiometries, and polymorphs, and validate our models with available experimental data. We use these thermodynamic models to make predictions for phase stability as a function of temperature, composition, and particle size. We provide insights for the influence of nanoparticle size on TMC nucleation and growth during synthesis. The theoretical framework utilized here provides a computationally-guided road map for navigating the rational synthesis of target TMC materials.

Contents

Acknowledgements

First of all, I would like to express my gratitude to my advisor, Prof. Paolucci, for his support, encouragement and guidance during my master’s study period. Despite being a master’s student, Prof. Paolucci trained me like a PhD student and gave me a PhD research project to investigate, which helped me develop systematic and coherent problem-solving abilities. I believe this will be valuable for my future career development. He also helped me with my English-speaking skills. Being an international student, I was poor at speaking English but, the weekly one-on-one meetings with him, and group presentations contributed immensely in improving my oral communication.

I would also like to thank Prof. Giri, a committee member, whose course on crystallization helped me understand important concepts that were applicable in my research. I’m also grateful to Prof. Choi, another committee member, whose course on advanced thermodynamics proved to be crucial for my project. I extend my gratitude to all the committee members for attending my thesis defense.

I also appreciate the help extended by my fellow members of the Paolucci group. I would like to thank Changming Liu for helping me debug codes and assisting with technical issues. I would like to thank Keka Mandal for guiding me through phase diagram plots. I would also like to acknowledge Anna Sviripa, Anukriti Shrestha, Asanka Wijerathne and Michael Schapowal for their valuable suggestions about my research. A special mention goes to Anukriti Shrestha and my friend Chen Cai, for correcting grammatical mistakes in my thesis.

Finally, I would like to thank my parents for their support and encouragement during my master’s period. I appreciate them for supporting my decision of pursuing a master’s degree abroad. Every time I would feel lonely, their video calls would motivate and comfort me. I would also like to thank my girlfriend for her mental support during my master’s program.

1. Introduction

Transition metal carbides (TMC) have been applied in various fields including heterogeneous catalysis, fuel cell, battery cathodes, cutting instruments and more.[1–4] The applications of TMCs are wide in part due to the diversity of their crystal structures and phase compositions. Understanding how to synthesize the desired phase is a necessary first step for utilizing the potential of TMCs. Among transition metal carbides, molybdenum carbides (Mo_xC, $x = 1, 2$) are an example that has been widely studied for their applications in catalysis. For example, α-Mo_2C has been used for the WGS reaction;[5,6] β-Mo_2C for hydrogenation of benzene,[7] hydrogenlysis of alkanes,[8] hydrodesulfurization (HDS),[9] hydrodenitrogenation (HDN),[10] and hydrodeoxygenation (HDO) reactions,[11] δ-MoC shows high activity and stability for dry reforming of methane (DRM),[12] and γ-MoC and η-MoC display potential for hydrogen evolution (HER).[13] Tungsten carbides (W_xC, $x =1, 2$) are another typical transition metal carbide that has been widely explored. δ-WC has been applied in polymer electrolyte membrane fuel cells,[14] hydrogenolysis of ethane and neopentane and in hydrodechlorination of chlorofluorocarbons,[15,16] β-W_2C has been utilized for catalyzing alkane hydrogenolysis reactions.[17] Unfortunately, there are no uniform methods to synthesize the different phases of TMC. The target transition metal carbide phases are synthesized using temperature-programmed reaction (TPR) methods at high temperatures and with different precursors[18–20] and there is no comprehensive theory that has been constructed for the TMC phase selection during the synthesis process.

Previous experimental studies demonstrated the stability of different TMC are affected by temperature and composition in the form of traditional thermodynamic phase diagrams extrapolated from a small number of experimental data.[21,22] In these phase diagrams and studies, the size of the TMC nanoparticles and their effect on phase stability are not reported. Other experimental papers have controlled for particle size and demonstrated it has measurable effects on phase boundaries for materials such as aluminas,[23] group IV semiconductors[24] and hematite nanoparticles.[25,26] Recently, computational thermodynamic models have been applied to describe relative stability of different phases as a function of particle size for manganese oxides and hydroxides.[27] These models offer guidance for the possible prediction of synthesis of different TMC phases by controlling nanoparticle size. Experiments have successfully synthesized TMCs with a narrow size distribution and particle sizes varying from ~1 nm to 100s of nm. For example Kim et al. utilized pyrolysis of metal organic frameworks (MOFs) to synthesis TMC nanoparticles of size ~4 nm.[28] Xu et al. utilized pyrolysis of zeolitic metal-azolate frameworks (MAFs) to synthesize tungsten carbide nanoparticles of ~2 nm.[29] Given the demonstrated experimental tunability of TMC particle size, a computationally-driven thermodynamic model that can predict the stability of different TMCs as a function of temperature, composition and nanoparticle size would be very valuable.

From classical nucleation theory, the synthesis of TMCs can be approximated as a crystallization process that obeys Ostwald's Rule,[30] where a variety of metastable TMCs nucleate and grow prior to the formation of the equilibrium phase if they have lower nucleation barrier than stable phases.[31,32] The relation of the nucleation barrier with surface energy and can be expressed as:

$$\Delta G_{\mathrm{c}} \propto \frac{(\eta\gamma)^3}{(-RTlnS)^2} \tag{1}$$

In this expression, $\eta\gamma$ represents the shape-averaged surface energy, and -RTln$S$ is the bulk thermodynamic driving force for crystallization. At small particle sizes, the nanoparticles exhibit large surface-area-to-volume ratios, causing the surface energy to dominate bulk energy. As a result, high-bulk-energy metastable phases with low surface energy can be thermodynamically stable at small nanoparticle sizes.[33,34] This theory has been confirmed for a series of metal-oxides by Navrotsky et al., who utilized experiments to demonstrate that many metastable polymorphs have lower surface energy than their stable bulk structures.[26] Combining the influence of surface energies with bulk energies at small nanoparticle sizes may be crucial for predicting phase-selection during the synthesis process.

In this work, we utilize density functional theory (DFT) to compute the bulk energy and surface energy for different molybdenum carbide and tungsten carbide phases. We construct a Gibbs free energy ΔG potential, as a function of particle size, to reveal how particle size affects the equilibrium phases. Initially, we ignore particle size and construct Gibbs free-energy diagrams for bulk TMC by varying chemical potential of transition metal and the chemical potential of carbon. The change of chemical potentials is then related to the temperature and the phase composition, which offers insights on how these synthetic variables influence the equilibrium phases. We next incorporate surface energies into the free-energy potential to construct a size-dependent phase diagram to predict how particle size influences equilibrium phases. Our theoretical work considers the stability of different phases as a function of temperature, phase composition and the particle size, which offers the predictive insights on how environmental conditions influence the phase equilibrium during the synthesis process and represents a novel predictive theory of TMC synthesis.

2. Methods

All density functional theory (DFT) calculations were conducted by Vienna Ab-Initio Software Package (VASP),[35] version 5.4.4. We used the projector augmented wave (PAW)[36,37] method of core valence interactions and a plane wave cutoff energy of 400 eV. The generalized gradient approximation(GGA) functional of Perdew, Burke, and Ernzerhof (PBE)[38] has been used to describe the exchange-correlation potential. We applied a minimum of 2.86 × 2.86 × 2.86 per Angstrom k-point density for all bulk structure optimizations (rounding up to the nearest integer), and a minimum of 2.86 × 2.86 × 1 per Angstrom (rounding up to the nearest integer) k-point density for all slab calculations. Cell vectors for bulk structures were optimized using ISIF=3. The convergence criterions for all calculations were electronic energies converged to 10^{-6} eV and atomic forces to less than 0.01 eV/Å. All of the initial bulk structures of transition metal carbides come from the Materials Project[39] and all of the slab constructions were performed by Python Materials Genomic (Pymatgen) package, *Slabgenerator* function.[40] To prevent the interaction between two adjacent surfaces, a vacuum space of 12 Å was added for each slab structure. The slabs contain six layers, with the bottom three layers fixed and not allowed to relax during optimization.

To explore the influence of surface energy on phase stability, we define surface energy as follows:

$$E_{sur} = (E_{slab} - nE_{bulk})/2A \tag{2}$$

where E_{sur}, E_{slab}, and E_{bulk} stand for the surface energy of the surface, the total energy of the slab model and the energy of a bulk structure respectively; n represents the number of bulk units in slab model; A represents the surface area. For a slab structure, there are two surfaces and they are the same, which is why the number 2 appears in the denominator.

We utilized DFT calculations with the same parameters described above to compute the bulk energy of reference molybdenum metal (space group Im-3m), tungsten metal (space group Im-3m) and graphene (space group $P6_3$/mmc). The bulk energy for Mo is E_{Mo} = -10.950 eV/atom, W is E_W = -13.016 eV/atom and C is E_C = -9.232 eV/atom.

The nanoparticle shapes were computed through numerical Wulff construction,[41] which is a method to determine the equilibrium crystal by minimizing the total surface energy. In our work, all of the nanoparticle shapes are established by the Wulffshape function of Pymatgen package code, which solves for the surface energy convex hull using different surfaces. The input of the Wulffshape function is the conventional unit cell and the corresponding list of miller index and surface energies.

3. Results and Discussion

3.1. Bulk Structures of Molybdenum Carbides (Mo_xC_y).

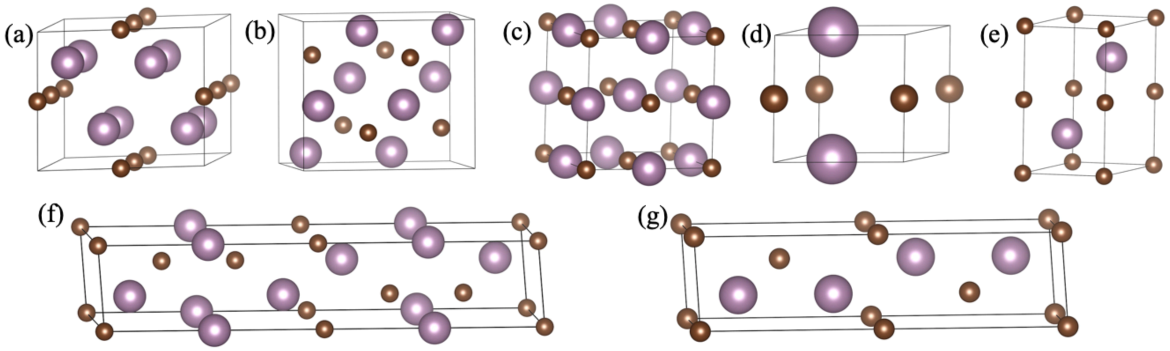

Figure 1. Bulk structures of molybdenum carbide in different phases. (a) β-Mo_2C, (b) α-Mo_2C, (c) δ-MoC, (d) γ-MoC, (e) G-MoC, (f) η-MoC, (g) γ'-MoC. Purple atoms are Mo, and brown C. Lines indicate the unit cell.

We explored seven different molybdenum carbide polymorphs and the atomic structures of the individual unit cells are displayed in Figure 1. The five MoC structures are δ-MoC, γ-MoC, G-MoC, η-MoC and γ'-MoC, shown in Figure 1c-g, respectively. The two Mo_2C phases are β-Mo_2C and α-Mo_2C, shown in Figure 1a-b, respectively. Initial structures were taken from the Materials Project[39] database and the initial G-MoC structure from Yu et al.[42] We used DFT calculations with the PBE functional to optimize cell shape, volume, atomic positions, and compute the bulk formation energy for each structure. The optimized structural parameters of different Mo_xC_y (x = 1, 2 and y = 1) phases, including cell parameters, space groups, and bulk energies are listed in Table 1. Lower bulk energies represent more stable Mo_xC_y structures. From Table 1, the α-Mo_2C is the most stable Mo_2C composition and γ-MoC is the most stable MoC composition, in agreement with previous experimental and computational results.[21]

β-Mo_2C (Figure 1a) displays a hexagonal close-packed (hcp) supercell) exhibiting an ABAB stacking sequence of the metal plane with carbon in the octahedral sites. For α-Mo_2C (Figure 1b), the atoms are in an orthorhombic structure in which C atoms occupy half octahedral interstitial sites available in one layer and the remaining octahedral sites in the next carbon layer. δ-MoC (Figure 1c) displays a NaCl-like face-centered cubic (fcc) structure, γ-MoC (Figure 1d) forms an alternating Mo and C layers with hexagonal close-packed (hcp) structure. G-MoC (Figure 1e) has staggered Mo atom in two layers along the *xy* plane and one more C layer between two adjacent Mo layers, η-MoC is a hexagonal structure with ABCABC stacking, and γ'-MoC(Figure 1g) also displays hcp structure with alternating two Mo and two C layers.

Table 1. The calculated cell parameters (a, b, c, in Å; V_{cell} in $Å^3$), bulk energy (eV/atom) of different Mo-C carbides (including δ-, γ-, G-, η-, γ'-MoC and β-, α-Mo_2Cpolymorphs).

Phase	β-Mo_2C	α-Mo_2C	δ-MoC	γ-MoC	G-MoC	η-MoC	γ'-MoC
S	$P\bar{3}m1$	Pbcn	$Fm\bar{3}m$	$P\bar{6}m2$	$P6_3/mmc$	$P6_3/mmc$	$P6_3/mmc$
a	3.059	4.739	4.375	2.918	2.959	3.075	3.000
b	3.059	6.061	4.375	2.918	2.959	3.075	3.000
c	4.661	5.232	4.375	2.828	5.422	15.337	10.804
V_{cell}	37.7836	150.2810	83.7522	20.8497	41.1038	125.6174	84.2234
E_{MoxCy}	-10.415	-10.482	-9.872	-10.182	-10.058	-9.924	-9.968

3.2. Molybdenum Carbide bulk phase diagram.

We next compute molybdenum carbide formation energies with reference to pure molybdenum and carbon sources (molybdenum metal and graphene):

$$x\mathrm{Mo} + y\mathrm{C} \rightarrow \mathrm{Mo}_x\mathrm{C}_y \tag{3}$$

$$\Delta E_{bulk} = (x+y)E_{\mathrm{Mo}x\mathrm{C}y} - xE_{\mathrm{Mo}} - yE_{c} \tag{4}$$

Here ΔE_{bulk} is the DFT-computed 0 K bulk formation energy of different molybdenum carbides relative to $Mo_{(s)}$ and $C_{(s)}$ references. In this expression, *x*, and *y* represent the number of Mo and C atoms in different molybdenum carbide phases (e.g. for β-Mo_2C, $x = 2$, $y = 1$). From the computational results, a thermodynamic phase diagram can be constructed. The bulk Gibbs free energy of different molybdenum carbides can be written in terms of chemical potentials for Mo and C:

$$\Delta G_{bulk}(\Delta\mu_{Mo}, \Delta\mu_{C}) = \Delta E_{bulk} - x\Delta\mu_{Mo} - y\Delta\mu_{C} \tag{5}$$

To construct a thermodynamic phase diagram, each phase is represented by a free-energy surface, $\Delta G_{bulk}(\Delta\mu_{Mo}, \Delta\mu_{C})$, as defined in equation (5). Fig 2a shows a 3-D phase diagram constructed by varying the chemical potentials $\Delta\mu_{Mo}$ and $\Delta\mu_{C}$. The different molybdenum carbide energy surfaces intersect with each other and determine the stable phases and their phase boundaries. By projecting the stability regions onto the $\Delta\mu_{Mo}$-$\Delta\mu_{C}$ plane as shown in Figure 2b, a 2-D bulk phase diagram can be established. Metastable phases, which are visualized in ΔG-$\Delta\mu_{Mo}$-$\Delta\mu_{C}$ 3-D diagram, do not show up on this 2-D phase diagram. The calculated results showed that γ-MoC is the most stable phase for the MoC composition, while the α-Mo_2C phase is the most stable for the Mo_2C composition.

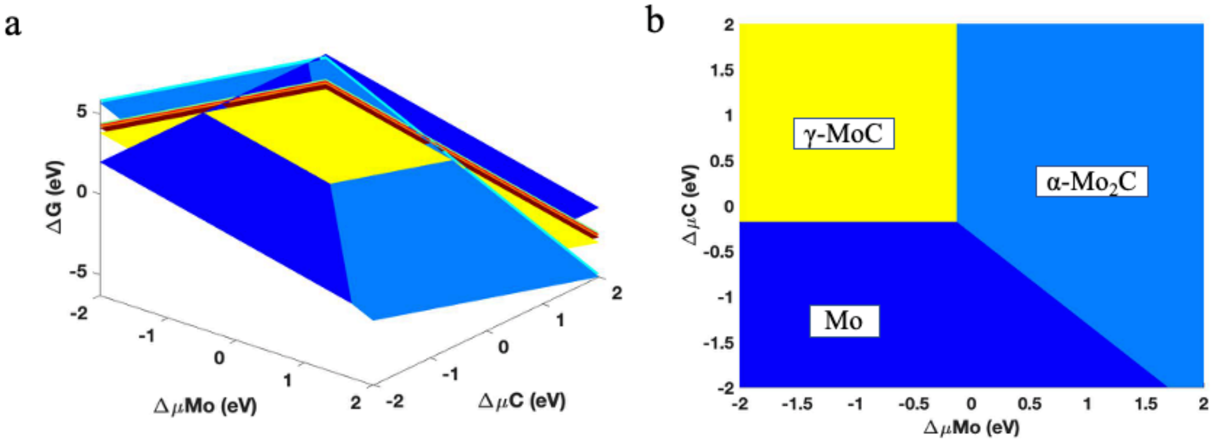

Figure 2. Bulk phase diagram of different molybdenum carbide phases. (a)3-D bulk phase diagram of different molybdenum carbide phases with the change of chemical potential. (b)Lowest-energy 2-D phase diagram by projecting 3-D diagram onto $\Delta\mu_{Mo}$-$\Delta\mu_{C}$ plane.

The $\Delta\mu$ are free parameters relative to the difference in chemical potential between 0 K and the actual condition. They can be related to corresponding temperatures and the composition through the ideal solution chemical potential relation[43]. We define X_c as the mole fraction of carbon, $X_c = \frac{\text{Mole C}}{\text{Mole C+Mole Mo}}$, the change of chemical potential can be written as:

$$\Delta\mu_{Mo}\,(T, X_c) = \mu^{\circ}_{Mo}(T) - \mu^{\circ}_{Mo}(0) + k_BT\ln(1-X_c) \qquad (6)$$

$$\Delta\mu_{C}\,(T, X_c) = \mu^{\circ}_{C}(T) - \mu^{\circ}_{C}(0) + k_BT\ln(X_c) \qquad (7)$$

$\mu^{\circ}_{Mo}(T)$ and $\mu^{\circ}_{C}(T)$ are the chemical potential of molybdenum and carbon at T and 0 K.

$$\Delta G^{\circ}(T) = \mu^{\circ}(T) - \mu^{\circ}(0) = [H^{\circ}(T) - H^{\circ}(Tr) - TS^{\circ}(T)] - [H^{\circ}(0) - H^{\circ}(Tr)] \qquad (8)$$

The change of chemical potential can be calculated from equation (8). In this expression, T represents the synthesized temperature; Tr is the reference temperature, which is 298.15K; H° and S° represent the standard enthalpy and entropy respectively. All of the thermodynamic data for H° and S° can was taken from the NIST-JANAF Thermodynamic Tables.[44] The new free energy potential in terms of these parameters is:

$$\Delta G_{bulk}(T, X_c) = \Delta E_{bulk} - x[\Delta G^{\circ}_{Mo}(T) + k_BT\ln(1-X_c)] - y[\Delta G^{\circ}_{C}(T) + k_BT\ln(X_c)] \qquad (9)$$

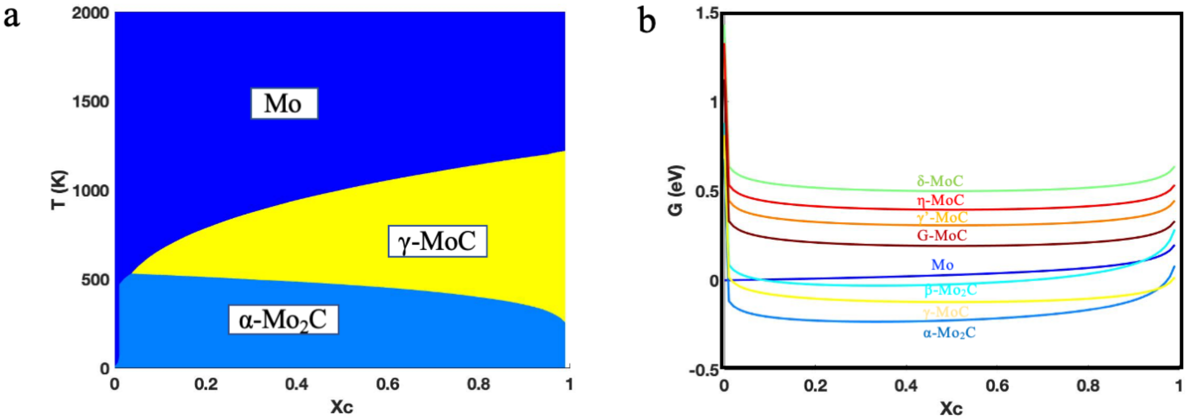

Figure 3. Traditional thermodynamic phase diagram of different molybdenum carbide phases. (a)Stability region of molybdenum carbide at different temperature and carbon composition. (b)Gibbs free-energy differences between various phases of molybdenum carbide at T=500K.

Figure 3a reports the phase diagram constructed using $\Delta G_{bulk}(T, X_c)$. At low temperature, when the carbon fraction in reactants is close to zero, pure Mo is the lowest free energy species. As the mole fraction of carbon increases, the stable phase will transfer from Mo to γ-MoC and α-Mo_2C. To assess the relative stability of other metastable phases we constructed a cross section of the phase diagram at 500 K (Figure 3b). The metastable β-Mo_2C phase has a small free energy difference of ~0.2 eV with α-Mo_2C. However, δ-MoC, η-MoC, γ'-MoC, G-MoC phases have substantially higher free energies compared to the stable α and γ phases. It may be hard to obtain these four metastable phases based on the bulk phase diagram.

3.3. Molybdenum Carbide nanoscale phase diagram.

The bulk phase diagrams in the previous section assume an infinite particle size. From classical nucleation theory, it is shown that metastable phases can be stabilized at the small particle size if they have lower surface energy than the equilibrium phases. We incorporated the surface energy term into the bulk free energy potential to obtain a size-dependent free energy potential as:[27]

$$\Delta G(r) = \Delta G_{bulk} + \left(\frac{1}{r}\right)\eta\rho\gamma \qquad (10)$$

In this expression, r is the effective[18] particle radius (nm), η is called shape factor without units (Area/Volume$^{2/3}$) of the equilibrium particle morphology, ρ is the volume normalized per mole of metal, and γ represents the averaged surface energy at the equilibrium phase.

We computed surface energies for all solid molybdenum carbides in Table 1 using the DFT slab calculation methods developed by Sun et al.[45,46] For each conventional molybdenum carbide bulk structure, miller-indices <3 and their different terminations have been enumerated and their DFT-optimized surface energies used to compute the Wulff construction for each phase.[47] The detailed results of surface calculation are summarized in Table 2. From the Wulff construction, the shape factor and average surface energy can be calculated. The equilibrium particle morphologies are shown in Figure 4. The calculated shape of the β-Mo$_2$C phase is only composed of 101 and 001 surfaces. Our calculated shape has been confirmed by Tang et al, who observed the same shape and miller index surfaces using TEM.[48] Our calculated cubic shape for δ-MoC is also consistent with TEM and XRD experiments.[49] For the other molybdenum carbide phases, we were unable to find experimental studies with the necessary resolution to identify nanoparticle shapes for comparison to our results.[13,18,50]

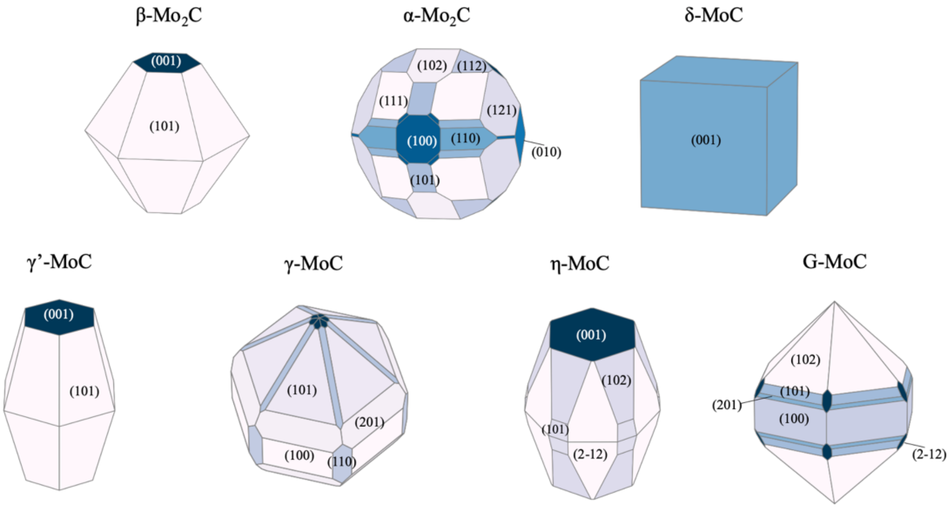

Figure 4. Computed Wulff Constructions of the equilibrium particle morphologies of different molybdenum carbide phases.

Table 2. The calculated surface parameters, shape factor η, volume ρ (Å^3/metal) and averaged surface energy (J/m^2)

Phase	Shape factor η	Volume ρ (Å^3/metal)	Surface energy γ (J/m^2)
Mo	4.95	15.89	2.920
β-Mo$_2$C	5.84	19.03	2.161
α-Mo$_2$C	5.05	18.93	2.977
δ-MoC	6.00	21.05	1.054
γ-MoC	5.08	20.85	3.417
G-MoC	5.56	21.06	3.361
η-MoC	5.26	20.94	2.754
γ'-MoC	5.14	20.55	2.841

The size-dependent free energy $\Delta G(\Delta\mu_{Mo}, \Delta\mu_C, 1/r)$, exists in a 4-D space, and can be projected onto the $\Delta\mu_{Mo}$-1/r axes at fixed $\Delta\mu_C$, or the $\Delta\mu_C$-1/r axes at fixed $\Delta\mu_{Mo}$, to construct size-dependent phase diagrams. To compare the energetic competition between molybdenum carbide phases at small nanoparticle size, a 3-D size-dependent phase diagram has been constructed at fixed $\Delta\mu_C$ = -0.025 eV in Figure 5a. $\Delta\mu_C$ = -0.025 eV is calculated at 500 K and X_c = 0.35, representative of common synthesis conditions.[19] The 2-D diagram of the stable region was constructed by projecting the 3-D diagram onto $\Delta\mu_{Mo}$-1/r plane as shown in Figure 5b. The metastable phase β-Mo_2C appears on the phase diagram at small particle size. As shown in Table 2, the averaged surface energy of β-Mo_2C is lower in energy than α-Mo_2C. At small particle sizes, the material will exhibit large surface-area to volume ratios, and in this case, the surface energy can be dominate over the bulk energy. Figure 5b predicts that β-Mo_2C is more likely to exist around 0.8~1.5nm. α-Mo_2C is more likely to be stable at the particle size larger than 1.5nm. This result is consistent with characterization of β-Mo_2C nanoparticles by Tang et al, who observed particle sizes <2 nm,[48] and facets in agreement with our Wulff shape. Reported α-Mo_2C particle sizes range from 1.21nm to 3.88nm[12,50] The experimental particle size results for α-Mo_2C are in reasonable agreement with the results in Figure 5b.

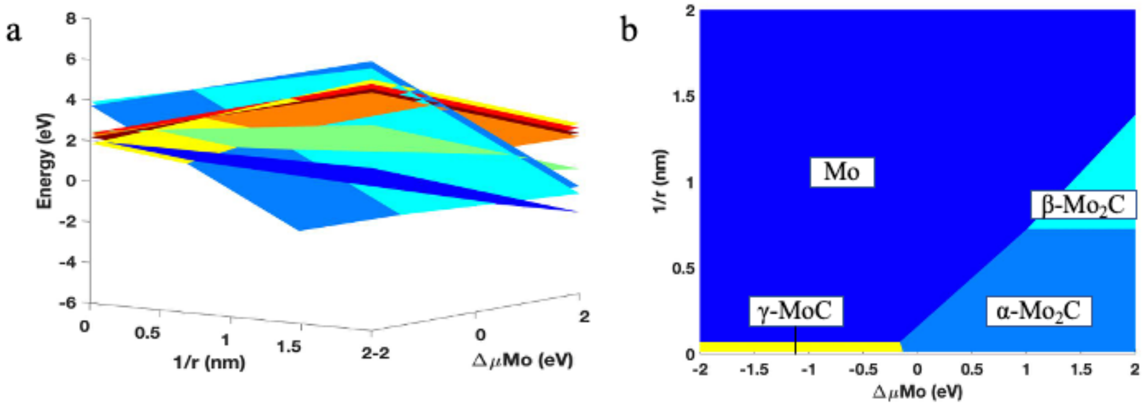

Figure 5. Size-dependent phase diagram of different molybdenum carbide phases at fixed $\Delta\mu_C$ = -0.025 eV. (a) 3-D bulk phase diagram of different molybdenum carbide phases with the change of chemical potential and the particle size. (b) Lowest-energy 2-D phase diagram by projecting 3-D diagram onto $\Delta\mu_{Mo}$-1/R plane.

We next used equation (10) to construct the size-dependent free energy as a function of temperature, phase composition and particle size $\Delta G(T, X_c, 1/r)$. Figure 6a shows a temperature size-dependent phase diagram constructed at X_c = 0.35. The metastable phase δ-MoC phase appears on the phase diagram with particle sizes <1.5nm. This result is consistent with the Liang et al.'s finding that the particle size of δ-MoC is 0.7-1.8 nm.[12] γ-MoC is more likely to be stable at a larger particle sizes, consistent with TEM observations for γ-MoC nanoparticle sizes of > 50 nm.[13] To compare the free energies of metastable phases we constructed a cross section of the phase diagram at 500 K (Figure 6b). As the particle size changes from small to large, the lowest free energy phase transfers from δ-MoC and β-Mo_2C to γ-MoC and α-Mo_2C.

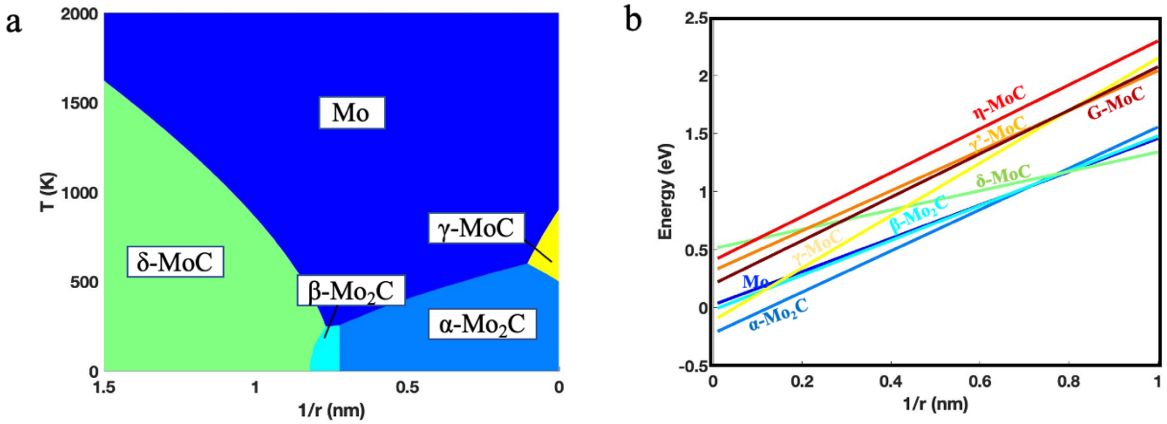

Figure 6. (a) Temperature Size-dependent phase diagram at Xc = 0.35. (b) Gibbs free-energy differences between various phases of molybdenum carbide at T=500K.

As shown in Table 3, the calculated surface energies of MoC polymorphs are ordered as $\gamma_{\delta\text{-MoC}} < \gamma_{\eta\text{-MoC}} < \gamma_{\gamma'\text{-MoC}} < \gamma_{\text{G-MoC}} < \gamma_{\gamma\text{-MoC}}$, and for the Mo_2C polymorphs, $\gamma_{\beta\text{-Mo2C}} < \gamma_{\alpha\text{-Mo2C}}$. The bulk energies of these phases are ordered in the opposite direction except for η-MoC and γ'-MoC. The metastable phases β-Mo_2C and δ-MoC appear on the size-dependent phase diagram but do not appear on the bulk phase diagram. Higher free energy metastable phases, such as η-MoC, are difficult to synthesize and few reports of their characterization exist. Our results predict, that given enough time η-MoC would relax into lower free energy phases. Tang et al. synthesized η-MoC by kinetically trapping it at 10 mins during pyrolysis; the same synthesis protocol taken to 20 mins formed the β-Mo_2C phase.[48]

3.4. Bulk Structure of Tungsten Carbides (W*x*C*y*).

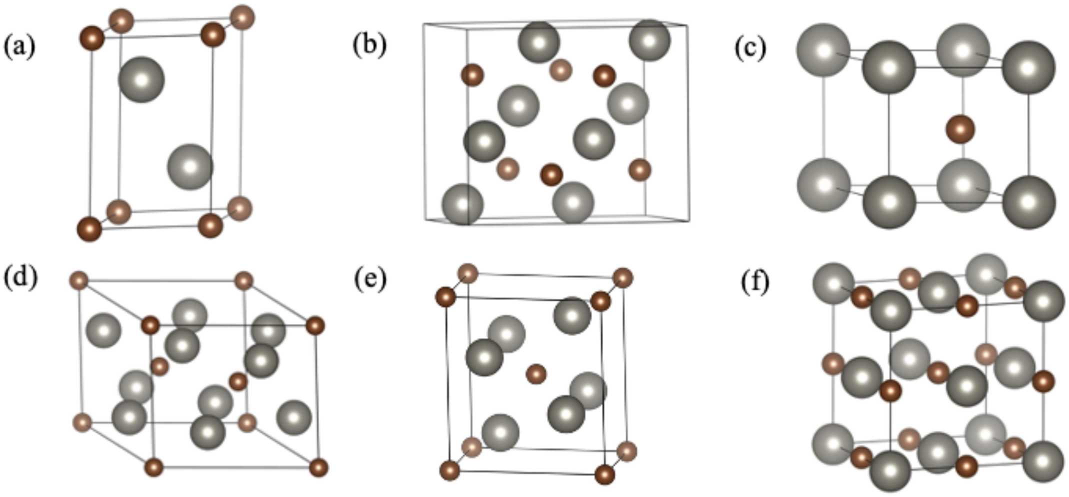

Figure 7. Bulk structures of tungsten carbide in different phases. (a) α-W_2C, (b) β-W_2C, (c) δ-WC, (d) ε-W_2C, (e) γ-W_2C, (f) γ-WC. Gray atoms are W and brown C. Lines indicate the unit cell

For the polymorphs of tungsten carbide, six different tungsten carbide structures were explored in this work, and their atomic structures and unit cells are displayed in Figure 7. All of the initial structures for different tungsten carbides came from the Materials Project database.[39] Table 3 reports the cell parameters following optimization of the cell shape, cell volume and atomic positions. The calculated parameters are consistent with available experimental data.[22,51]

Table 3. The calculated cell parameters (a, b, c, in Å; V_{cell} in Å^3), bulk energies (eV/atom) of different W-C carbides (including δ-, γ-WC and α-, β-, ε, γ-W_2C polymorphs).

Phase	α-W_2C	β-W_2C	δ-WC	ε-W_2C	γ-W_2C	γ-WC
Space group	$P\bar{3}m1$	Pbcn	$P\bar{6}m2$	$P\bar{3}1m$	$P6_3/mmc$	$Fm\bar{3}m$
a	3.070	4.756	2.928	5.257	3.034	4.385
b	3.070	6.111	2.928	5.257	6.103	4.385
c	4.678	5.237	2.853	4.799	4.740	4.385
V_{cell}	37.8533	150.7198	20.9939	113.3209	75.3234	83.9153
$E_{W_xC_y}$	-11.696	-11.770	-11.260	-11.754	-11.765	-10.803

3.5. Tungsten Carbide bulk phase diagram

Similar to Mo_xC_y, for tungsten carbides we define the reaction for carbide formation as:

$$xW + yC \rightarrow W_xC_y \tag{11}$$

$$\Delta E_{bulk} = (x+y)E_{W_xC_y} - xE_W - yE_C \tag{12}$$

We computed the bulk energy $\Delta E_{W_xC_y}$ of different tungsten carbide phases and displayed them in Table 3. The Gibbs free-energy potential for tungsten carbides can be expressed as:

$$\Delta G_{bulk}(\Delta\mu_W, \Delta\mu_C) = \Delta E_{bulk} - x\Delta\mu_W - y\Delta\mu_C \quad (13)$$

We applied the same methods used to generate Figure 2 to tungsten carbides and constructed the bulk phase diagram by varying the chemical potential of W and C as shown in Figure 8. The bulk phase diagram shows that δ-WC is the most stable phase for the WC composition and β-W_2C is the most stable phase for the W_2C composition.

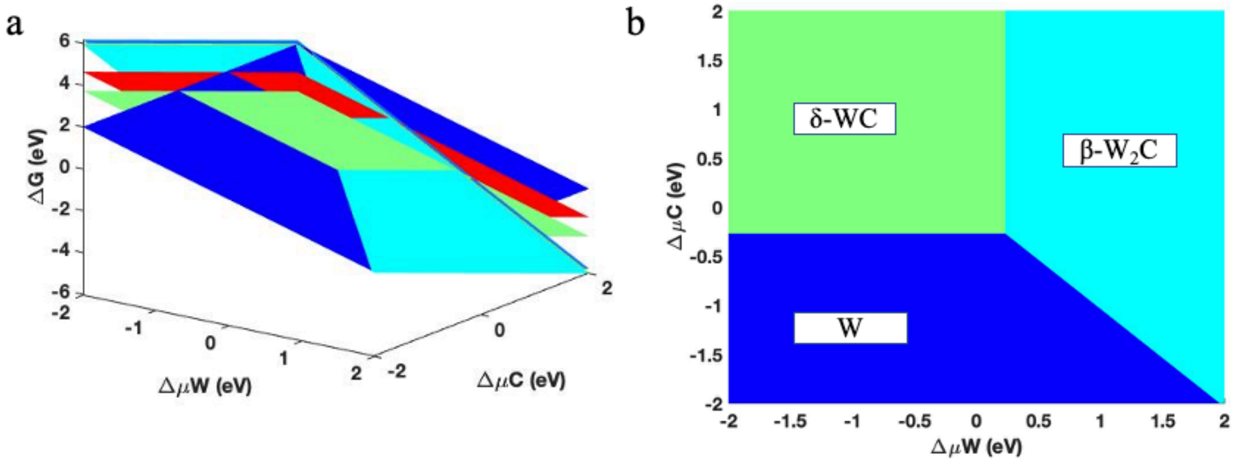

Figure 8. Bulk phase diagram of different tungsten carbide phases. (a)3-D bulk phase diagram of different tungsten carbide phases with the change of chemical potential. (b)Lowest-energy 2-D phase diagram by projecting 3-D diagram onto $\Delta\mu_W$-$\Delta\mu_C$ plane.

Using the same process as for molybdenum carbide phase diagram, the change of chemical potential can be related to temperature and the mole fraction of carbon in the reactants. Therefore, the bulk Gibbs free-energy potential can be transferred as:

$$\Delta G_{bulk}(T, X_c) = \Delta E_{bulk} - x[\Delta G^\circ_W(T) + k_BT\ln(1\text{-}X_c)] - y[\Delta G^\circ_C(T) + k_BT\ln(X_c)] \quad (14)$$

Fig 9a shows the bulk thermodynamic phase diagram constructed from equation (14). At low temperature, when the carbon mole fraction is close to zero, the W metal is the most stable phase. As the percentage of carbon increases, the stable phase transitions from W to δ-WC. We constructed the Gibbs free-energy cross-section diagram at 500K shown in Figure 9b. For β-W_2C, ε-W_2C, γ-W_2C, and δ-WC free energy differences are small and span ~0.3 eV. γ-WC and α-WC phases have higher free energy differences. Therefore, it would be more difficult to synthesize the γ-WC and α-WC phases based on the bulk phase diagram.

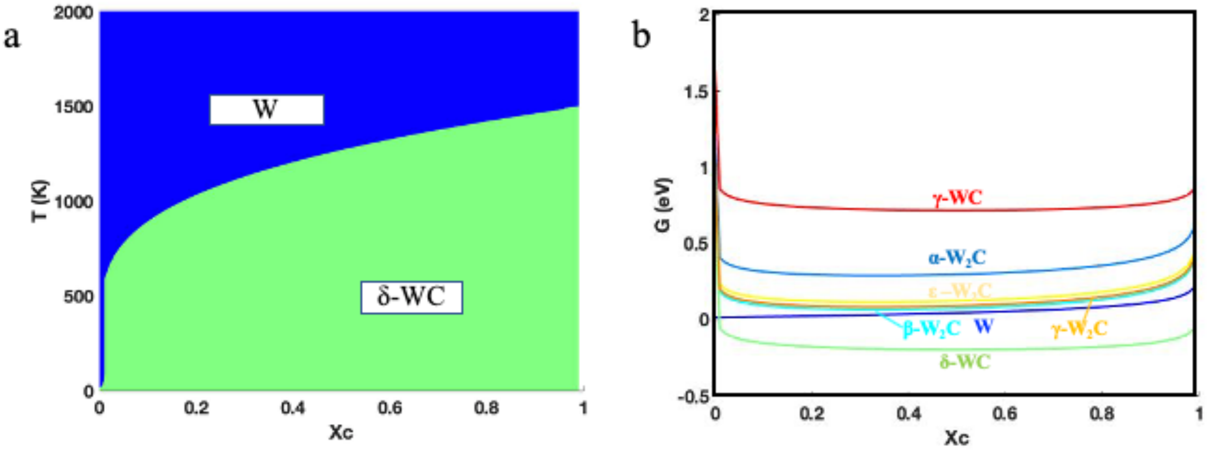

Figure 9. Traditional thermodynamic phase diagram of different tungsten carbide phases. (a)Stability region of tungsten carbide at different temperature and carbon composition. (b)Gibbs free-energy differences between various phases of tungsten carbide at T=500K.

3.6. Tungsten Carbide nanoscale phase diagram

Similar to Mo_xC_y, we next computed surface energies for all tungsten carbides using DFT slab calculations, and constructed their corresponding Wulff shapes, shown in Figure 10. The detailed results for surface calculation are summarized in Table 4.

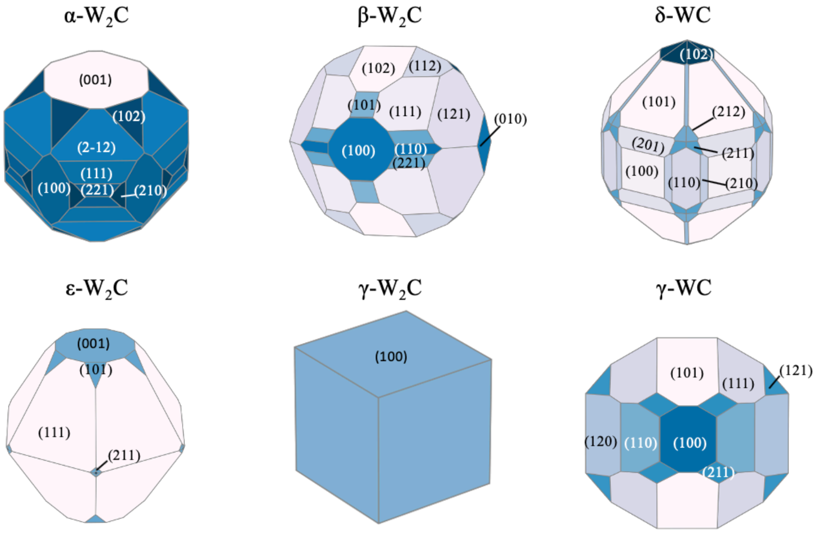

Figure 10. Computed Wulff Constructions of the equilibrium particle morphologies of different tungsten carbide phases.

Table 4. The calculated surface parameters, shape factor η, volume ρ (Å^3/metal) and averaged surface energy γ (J/m^2)

Phase	Shape factor η	Volume ρ (Å^3/metal)	Surface energy γ (J/m^2)
W	5.00	16.19	3.34
α-W$_2$C	5.02	18.93	3.26
β-W$_2$C	5.08	18.84	3.09

δ-WC	5.01	20.99	4.00
ε-W_2C	5.24	18.89	2.77
γ-W_2C	5.14	18.83	3.01
γ-WC	6.00	20.98	1.03

We applied equation (10) to construct the size-dependent phase diagram of tungsten carbides as shown in Figure 11. From Figure 11b, the metastable phase ε-W_2C now appears on the phase diagram and it is more likely to exist around 0.8~2.5nm. The size-dependent phase diagram also shows that the β-W_2C is more likely to be stable at particle sizes larger than 2.5nm.

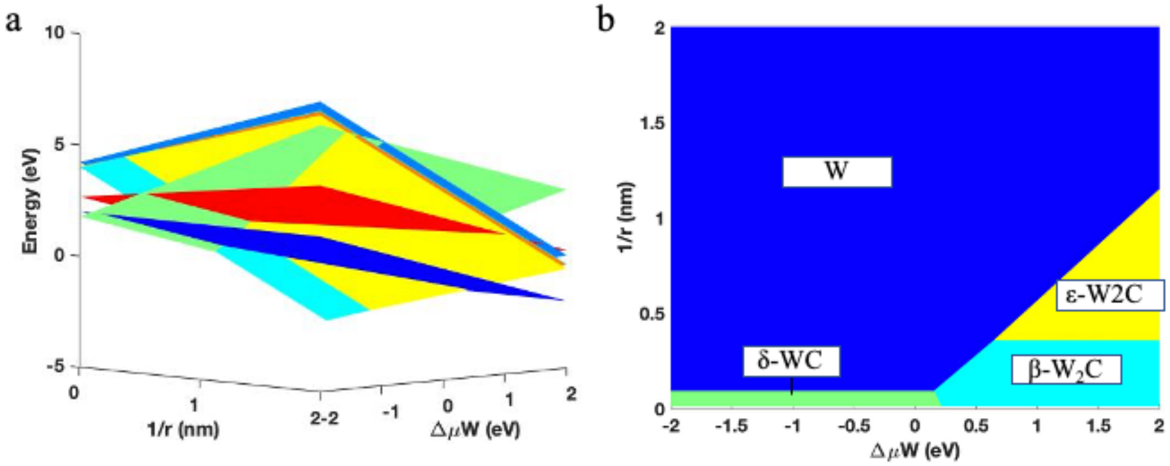

Figure 11. Size-dependent phase diagram of different tungsten carbide phases at fixed $\Delta\mu_C = -0.025$ eV. (a) 3-D bulk phase diagram of different tungsten carbide phases with the change of $\Delta\mu_W$ and the particle size. (b) Lowest-energy 2-D phase diagram by projecting 3-D diagram onto $\Delta\mu_W$-1/R plane.

By applying the same methodology as in Figure 6, we constructed a size-dependent phase diagram for tungsten carbides as a function of temperature, composition and particle size. Figure 12a shows size-dependent phase diagram at fixed $X_c = 0.35$. The γ-WC phase appears on the phase diagram with particle sizes <1.5nm. δ-WC is stable at large particle sizes. Giordano et al. synthesized δ-WC nanoparticles and observed particle sizes were > 4nm.[52] This result agrees with the prediction in Figure 12a. We constructed a cross section of the phase diagram at 500 K (Figure 12b) to compare the free energy differences of different metastable phases. When the particle size is between 1.5nm ~ 4nm, the energy differences between W_2C and W are very small. Therefore, it is a reasonable prediction that β-W_2C, ε-W_2C, and γ-W_2C, are all likely phases at 1.5 ~ 4nm, with δ -WC dominating at much larger particle sizes.

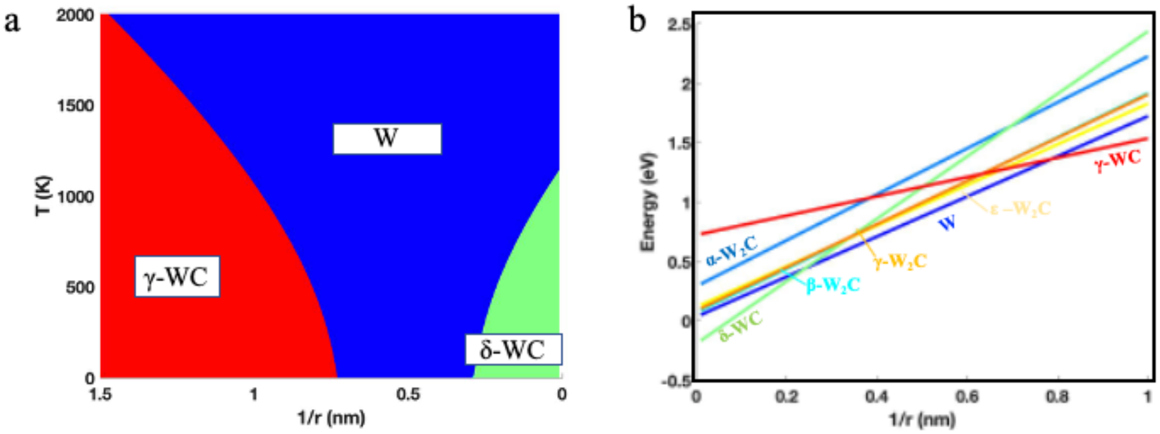

Figure 12. (a) Temperature Size-dependent phase diagram at Xc = 0.35. (b) Gibbs free-energy differences between various phases of molybdenum carbide at T=500K

4. Conclusions

In this thesis, we utilized DFT calculations to compute bulk formation energies and surface energies of multiple TMC polymorphs. Combing these with classical nucleation theory and Wulff constructions, we formulated theoretical size-dependent phase diagrams that incorporate nanoscale effects. Our theoretical framework provides guidance for the influence of variations in synthesis conditions on the stability of non-equilibrium phases and provides insights on the intermediate phase transitions.

There are two points to extend my thesis for future work. The first point is that we can compute the particle size-dependent phase diagrams for other commonly used TMCs, such as vanadium carbide, which also has different polymorphs and is used as a catalyst. The other point is that we can adjust the surface energies of different TMC phases by adsorption of other species that may be incorporated during synthesis. As we demonstrate here, the stability of multiple phases for TMCs strongly depend on surface energies. Surface energies can be controlled by the addition of other chemicals and would result in a new size-dependent phase diagram that potentially reveals other metastable phases. In this case, our theoretical framework could offer useful insights into the promoters and particle sizes that would result in favorable free energies of target meta-stable phases.

References

(1) Levy, R. B.; Boudart, M. Platinum-like Behavior of Tungsten Carbide in Surface Catalysis. *Science (80-.).* **1973**, *181* (4099), 547–549. https://doi.org/10.1126/science.181.4099.547.

(2) Hwu, H. H.; Chen, J. G. Surface Chemistry of Transition Metal Carbides. *Chem. Rev.* **2005**, *105* (1), 185–212. https://doi.org/10.1021/cr0204606.

(3) Ham, D. J.; Lee, J. S. Transition Metal Carbides and Nitrides as Electrode Materials for Low Temperature Fuel Cells. *Energies* **2009**, *2* (4), 873–899. https://doi.org/10.3390/en20400873.

(4) Kimmel, Y. C.; Xu, X.; Yu, W.; Yang, X.; Chen, J. G. Trends in Electrochemical Stability of Transition Metal Carbides and Their Potential Use as Supports for Low-Cost Electrocatalysts. *ACS Catal.* **2014**, *4* (5), 1558–1562. https://doi.org/10.1021/cs500182h.

(5) Nagai, M.; Matsuda, K. Low-Temperature Water-Gas Shift Reaction over Cobalt-Molybdenum Carbide Catalyst. *J. Catal.* **2006**, *238* (2), 489–496. https://doi.org/10.1016/j.jcat.2006.01.003.

(6) Schaidle, J. A.; Lausche, A. C.; Thompson, L. T. Effects of Sulfur on Mo2C and Pt/Mo2C Catalysts: Water Gas Shift Reaction. *J. Catal.* **2010**, *272* (2), 235–245. https://doi.org/10.1016/j.jcat.2010.04.004.

(7) JAE S. LEE, 1 MI H. YEOM, KI. Y. PARK, IN-SIK NAM, JONG S. CHUNG , YOUNG G. KIM, A. S. H. M. Preparation and Benzene Hydrogenation Activity of Supported Molybdenum Carbide Catalysts. *J. Catal.* **1991**, *128*, 126–136.

(8) Lee, J. S.; Locatelli, S.; Oyama, S. T.; Boudart, M. Molybdenum Carbide Catalysts 3. Turnover Rates for the Hydrogenolysis of n-Butane. *J. Catal.* **1990**, *125* (1), 157–170. https://doi.org/10.1016/0021-9517(90)90086-Y.

(9) Sundaramurthy, V.; Dalai, A. K.; Adjaye, J. HDN and HDS of Different Gas Oils Derived from Athabasca Bitumen over Phosphorus-Doped NiMo/γ-Al2O3 Carbides. *Appl. Catal. B Environ.* **2006**, *68* (1–2), 38–48. https://doi.org/10.1016/j.apcatb.2006.07.014.

(10) Al-Megren, H. A.; González-Cortés, S. L.; Xiao, T.; Green, M. L. H. A Comparative Study of the Catalytic Performance of Co-Mo and Co(Ni)-W Carbide Catalysts in the Hydrodenitrogenation (HDN) Reaction of Pyridine. *Appl. Catal. A Gen.* **2007**, *329*, 36–45. https://doi.org/10.1016/j.apcata.2007.06.013.

(11) Ramanathan, S.; Oyama, S. T. New Catalysts for Hydroprocessing: Transition Metal Carbides and Nitrides. *J. Phys. Chem.* **1995**, *99* (44), 16365–16372. https://doi.org/10.1021/j100044a025.

(12) Liang, P.; Gao, H.; Yao, Z.; Jia, R.; Shi, Y.; Sun, Y.; Fan, Q.; Wang, H. Simple Synthesis of Ultrasmall β-Mo2C and α-MoC1-x Nanoparticles and New Insights into Their Catalytic Mechanisms for Dry Reforming of Methane. *Catal. Sci. Technol.* **2017**, *7* (15), 3312–3324. https://doi.org/10.1039/c7cy00708f.

(13) Wan, C.; Regmi, Y. N.; Leonard, B. M. Multiple Phases of Molybdenum Carbide as Electrocatalysts for the Hydrogen Evolution Reaction. *Angew. Chemie - Int. Ed.* **2014**, *53* (25), 6407–6410. https://doi.org/10.1002/anie.201402998.

(14) Wu, M.; Lin, X.; Hagfeldt, A.; Ma, T. Low-Cost Molybdenum Carbide and Tungsten Carbide Counter Electrodes for Dye-Sensitized Solar Cells. *Angew. Chemie - Int. Ed.* **2011**, *50* (15), 3520–3524. https://doi.org/10.1002/anie.201006635.

(15) Oyama, S. T. Preparation and Catalytic Properties of Transition Metal Carbides and Nitrides. *Catal. Today* **1992**, *15* (2), 179–200. https://doi.org/10.1016/0920-5861(92)80175-M.

(16) Delannoy, L.; Giraudon, J. M.; Granger, P.; Leclercq, L.; Leclercq, G. Group VI Transition Metal Carbides as Alternatives in the Hydrodechlorination of Chlorofluorocarbons. *Catal. Today* **2000**, *59* (3), 231–240. https://doi.org/10.1016/S0920-5861(00)00289-3.

(17) Ribeiro, F. H.; Boudart, M.; Dalla Betta, R. A.; Iglesia, E. Catalytic Reactions of N-Alkanes on β-W2C and WC: The Effect of Surface Oxygen on Reaction Pathways. *J. Catal.* **1991**, *130* (2), 498–513. https://doi.org/10.1016/0021-9517(91)90131-M.

(18) Reddy, K. M.; Rao, T. N.; Revathi, J.; Joardar, J. Structural Stability of α/β-Mo2C during Thermochemical Processing. *J. Alloys Compd.* **2010**, *494* (1–2), 386–391. https://doi.org/10.1016/j.jallcom.2010.01.055.

(19) Shohoji, N.; Badie, J. M.; Granier, B.; Costa Oliveira, F. A.; Fernandes, J. C.; Rosa, L. G. Formation of Hexagonal η-MoC1-x Phase at a Temperature Lower than 1660 °C by Solar Radiation Heating under Presence of Excess Free Carbon. *Int. J. Refract. Met. Hard Mater.* **2007**, *25* (3), 220–225. https://doi.org/10.1016/j.ijrmhm.2006.05.004.

(20) Rees, E. J.; Brady, C. D. A.; Burstein, G. T. Solid-State Synthesis of Tungsten Carbide

from Tungsten Oxide and Carbon, and Its Catalysis by Nickel. *Mater. Lett.* **2008**, *62* (1), 1–3. https://doi.org/10.1016/j.matlet.2007.04.088.

(21) Hugosson, H. W.; Eriksson, O.; Nordström, L.; Jansson, U.; Fast, L.; Delin, A.; Wills, J. M.; Johansson, B. Theory of Phase Stabilities and Bonding Mechanisms in Stoichiometric and Substoichiometric Molybdenum Carbide. *J. Appl. Phys.* **1999**, *86* (7), 3758–3767. https://doi.org/10.1063/1.371284.

(22) Kurlov, A. S.; Gusev, A. I. Phase Equilibria in the W–C System and Tungsten Carbides. *Russ. Chem. Rev.* **2006**, *75* (7), 617–636. https://doi.org/10.1070/rc2006v075n07abeh003606.

(23) McHale, J. M.; Auroux, A.; Perrotta, A. J.; Navrotsky, A. Surface Energies and Thermodynamic Phase Stability in Nanocrystalline Aluminas. *Science (80-.).* **1997**, *277* (5327), 788–789. https://doi.org/10.1126/science.277.5327.788.

(24) Barnard, A. S.; Zapol, P. A Model for the Phase Stability of Arbitrary Nanoparticles as a Function of Size and Shape. *J. Chem. Phys.* **2004**, *121* (9), 4276–4283. https://doi.org/10.1063/1.1775770.

(25) He, Y. T.; Wan, J.; Tokunaga, T. Kinetic Stability of Hematite Nanoparticles: The Effect of Particle Sizes. *J. Nanoparticle Res.* **2008**, *10* (2), 321–332. https://doi.org/10.1007/s11051-007-9255-1.

(26) Navrotsky, A. Nanoscale Effects on Thermodynamics and Phase Equilibria in Oxide Systems. *ChemPhysChem* **2011**, *12* (12), 2207–2215. https://doi.org/10.1002/cphc.201100129.

(27) Sun, W.; Kitchaev, D. A.; Kramer, D.; Ceder, G. Non-Equilibrium Crystallization Pathways of Manganese Oxides in Aqueous Solution. *Nat. Commun.* **2019**, *10* (1), 1–9. https://doi.org/10.1038/s41467-019-08494-6.

(28) Kim, J.; McNamara, N. D.; Her, T. H.; Hicks, J. C. Carbothermal Reduction of Ti-Modified IRMOF-3: An Adaptable Synthetic Method to Support Catalytic Nanoparticles on Carbon. *ACS Appl. Mater. Interfaces* **2013**, *5* (21), 11479–11487. https://doi.org/10.1021/am404089v.

(29) Xu, Y. T.; Xiao, X.; Ye, Z. M.; Zhao, S.; Shen, R.; He, C. T.; Zhang, J. P.; Li, Y.; Chen, X. M. Cage-Confinement Pyrolysis Route to Ultrasmall Tungsten Carbide Nanoparticles for Efficient Electrocatalytic Hydrogen Evolution. *J. Am. Chem. Soc.* **2017**, *139* (15),

5285–5288. https://doi.org/10.1021/jacs.7b00165.

(30) Ostwald, W. Studien Über Die Bildung Und Umwandlung Fester Körper. *Zeitschrift für Phys. Chemie* **2017**, *22U* (1). https://doi.org/10.1515/zpch-1897-2233.

(31) Navrotsky, A. Energetic Clues to Pathways to Biomineralization: Precursors, Clusters, and Nanoparticles. *Proc. Natl Acad. Sci.* **2004**, *101*, 12096–12101.

(32) Sun, W.; Ceder, G. Induction Time of a Polymorphic Transformation. *CrystEngComm* **2017**, *19* (31), 4576–4585. https://doi.org/10.1039/c7ce00766c.

(33) Sun, W.; Jayaraman, S.; Chen, W.; Persson, K. A.; Ceder, G. Nucleation of Metastable Aragonite CaCO 3 in Seawater. *Proc. Natl. Acad. Sci. U. S. A.* **2015**, *112* (11), 3199–3204. https://doi.org/10.1073/pnas.1423898112.

(34) Kitchaev, D. A.; Ceder, G. Evaluating Structure Selection in the Hydrothermal Growth of FeS 2 Pyrite and Marcasite. *Nat. Commun.* **2016**, *7*, 1–7. https://doi.org/10.1038/ncomms13799.

(35) Kresse, G.; Furthmüller, J. Efficient Iterative Schemes for Ab Initio Total-Energy Calculations Using a Plane-Wave Basis Set. *Phys. Rev. B - Condens. Matter Mater. Phys.* **1996**, *54* (16), 11169–11186. https://doi.org/10.1103/PhysRevB.54.11169.

(36) Joubert, D. From Ultrasoft Pseudopotentials to the Projector Augmented-Wave Method. *Phys. Rev. B - Condens. Matter Mater. Phys.* **1999**, *59* (3), 1758–1775. https://doi.org/10.1103/PhysRevB.59.1758.

(37) Blöchl, P. E. Projector Augmented-Wave Method. *Phys. Rev. B* **1994**, *50* (24), 17953–17979. https://doi.org/10.1103/PhysRevB.50.17953.

(38) Perdew, J. P.; Burke, K.; Ernzerhof, M. Generalized Gradient Approximation Made Simple. *Phys. Rev. Lett.* **1996**, *77* (18), 3865–3868. https://doi.org/10.1103/PhysRevLett.77.3865.

(39) Jain, A.; Ong, S. P.; Hautier, G.; Chen, W.; Richards, W. D.; Dacek, S.; Cholia, S.; Gunter, D.; Skinner, D.; Ceder, G.; Persson, K. A. Commentary: The Materials Project: A Materials Genome Approach to Accelerating Materials Innovation. *APL Mater.* **2013**, *1* (1). https://doi.org/10.1063/1.4812323.

(40) Ong, S. P.; Richards, W. D.; Jain, A.; Hautier, G.; Kocher, M.; Cholia, S.; Gunter, D.; Chevrier, V. L.; Persson, K. A.; Ceder, G. Python Materials Genomics (Pymatgen): A Robust, Open-Source Python Library for Materials Analysis. *Comput. Mater. Sci.* **2013**,

68, 314–319. https://doi.org/10.1016/j.commatsci.2012.10.028.

(41) Wulff, G. XXY . Zur Frage Der Geschwindigkeit Des Wachs-. *Zeitschrift Für Krist. - Cryst. Mater.* **1901**, 449–530.

(42) Yu, G. Q.; Huang, B. Y.; Chen, X.; Wang, D.; Zheng, F.; Li, X. B. Uncovering the Surface and Phase Effect of Molybdenum Carbides on Hydrogen Evolution: A First-Principles Study. *J. Phys. Chem. C* **2019**, *123* (36), 21878–21887. https://doi.org/10.1021/acs.jpcc.9b04461.

(43) Paula, P. A. and J. de. *Atkins' Physical Chemistry*; 2006.

(44) Jr, M. C. NIST-JANAF Thermochemical Tables. *J. Phys. Chem. Ref. Data, Monogr.* **1998**.

(45) Sun, W.; Ceder, G. Efficient Creation and Convergence of Surface Slabs. *Surf. Sci.* **2013**, *617*, 53–59. https://doi.org/10.1016/j.susc.2013.05.016.

(46) Sun, W.; Ceder, G. A Topological Screening Heuristic for Low-Energy, High-Index Surfaces. *Surf. Sci.* **2018**, *669* (November 2017), 50–56. https://doi.org/10.1016/j.susc.2017.11.007.

(47) Dobrushin, R. L.; Kotecký, R.; Shlosman, S. B. Wulff Construction: A Global Shape from Local Interaction. *Transl. Math. Monogr.* **1992**, *104* (January 1992), 189.

(48) Tang, C.; Sun, A.; Xu, Y.; Wu, Z.; Wang, D. High Specific Surface Area Mo2C Nanoparticles as an Efficient Electrocatalyst for Hydrogen Evolution. *J. Power Sources* **2015**, *296*, 18–22. https://doi.org/10.1016/j.jpowsour.2015.07.016.

(49) Hare, J. P.; Hsu, W. K.; Kroto, H. W.; Lappas, A.; Prassides, K.; Terrones, M.; Walton, D. R. M. Nanoscale Encapsulation of Molybdenum Carbide in Carbon Clusters. *Chem. Mater.* **1996**, *8* (1), 6–8. https://doi.org/10.1021/cm950339y.

(50) Alhajri, N. S.; Anjum, D. H.; Takanabe, K. Molybdenum Carbide-Carbon Nanocomposites Synthesized from a Reactive Template for Electrochemical Hydrogen Evolution. *J. Mater. Chem. A* **2014**, *2* (27), 10548–10556. https://doi.org/10.1039/c4ta00577e.

(51) Li, Y.; Gao, Y.; Xiao, B.; Min, T.; Fan, Z.; Ma, S.; Xu, L. Theoretical Study on the Stability, Elasticity, Hardness and Electronic Structures of W-C Binary Compounds. *J. Alloys Compd.* **2010**, *502* (1), 28–37. https://doi.org/10.1016/j.jallcom.2010.04.184.

(52) Giordano, C.; Erpen, C.; Yao, W.; Antonietti, M. Synthesis of Mo and W Carbide and

Nitride Nanoparticles via a Simple “Urea Glass” Route. *Nano Lett.* **2008**, *8* (12), 4659–4663. https://doi.org/10.1021/nl8018593.